Satellite-Observed Precipitation Response to Ocean Mesoscale Eddies

XUE LIU

Department of Oceanography, Texas A&M University, College Station, Texas, and Physical Oceanography Laboratory, Collaborative Innovation Center of Marine Science and Technology, Ocean University of China, and Qingdao National Laboratory for Marine Science and Technology, Qingdao, China

PING CHANG

Department of Oceanography, and Department of Atmospheric Sciences, Texas A&M University, College Station, Texas, and Physical Oceanography Laboratory, Collaborative Innovation Center of Marine Science and Technology, Ocean University of China, and Qingdao National Laboratory for Marine Science and Technology, Qingdao, China

JAISON KURIAN

Department of Oceanography, Texas A&M University, College Station, Texas

R. SARAVANAN

Department of Atmospheric Sciences, Texas A&M University, College Station, Texas

XIAOPEI LIN

Physical Oceanography Laboratory, Collaborative Innovation Center of Marine Science and Technology, Ocean University of China, and Qingdao National Laboratory for Marine Science and Technology, Qingdao, China

(Manuscript received 5 October 2017, in final form 2 May 2018)

ABSTRACT

Among various forms of atmospheric response to ocean mesoscale eddies, the rainfall response is the most difficult to quantify and is subject to considerable uncertainty. Here the robustness of the rainfall response is examined by comparing three different satellite-derived rainfall datasets: the Tropical Rainfall Measuring Mission (TRMM) Multisatellite Precipitation Analysis (TMPA), NOAA Climate Prediction Center (CPC) morphing technique (CMORPH) global precipitation, and the newly available Integrated Multisatellite Retrievals for Global Precipitation Measurement (IMERG) that is based on the latest remote sensing technology with finer spatial and temporal resolution. Results show that all datasets exhibit a similar rainfall response to ocean eddies, but the amplitude of the rainfall response is much stronger in IMERG than in the other two, despite the fact that IMERG provides the weakest time-mean rainfall estimate. In situ validation against the NOAA's Ocean Climate Stations Project (OCS) Kuroshio Extension Observatory (KEO) buoy rainfall measurement shows that IMERG is more accurate in estimating both the mean value of rainfall and its intensity distribution than the other two products, at least in the Kuroshio Extension region. Further analysis reveals that 1) eddy-induced precipitation response is significantly stronger in winter than in summer, and 2) warm-eddy-induced rainfall response is considerably stronger than cold-eddy-induced response, and these asymmetries in rainfall response are more robust in IMERG than in the other two datasets. Documenting and analyzing these asymmetric rainfall responses is important for understanding the potential role of ocean eddies in forcing the large-scale atmospheric circulation and climate.

1. Introduction

Ocean mesoscale eddies can make a significant contribution to sea surface temperature (SST) variability along western boundary current regimes, such as the Kuroshio Extension (e.g., Ma et al. 2016), where eddies are energetic and frontal-mesoscale air–sea interactions are intense. Over the past decade, noteworthy progress in satellite measurements has produced a suite of high-resolution observations that allow for the identification of active coupling between ocean mesoscale eddies and atmosphere (OME-A; Chelton et al. 2004; Xie 2004;

Corresponding author: Xue Liu, xuetamu@gmail.com

DOI: 10.1175/JCLI-D-17-0668.1

Small et al. 2008; Bryan et al. 2010; Chelton and Xie 2010; O'Neill et al. 2010, 2012; Frenger et al. 2013; Ma et al. 2016). One clear manifestation of this ocean–atmosphere coupling is the remarkable positive correlation between mesoscale SST and wind speed over major ocean fronts, such as the Gulf Stream, Kuroshio, Agulhas Return Current, and Brazil–Malvinas Confluence (Chelton et al. 2004; Park et al. 2006; O'Neill et al. 2005; Tokinaga et al. 2005; Bryan et al. 2010; O'Neill et al. 2010, 2012). Recent studies (Frenger et al. 2013; J. Ma et al. 2015; Byrne et al. 2015) further show that atmospheric response to eddy-induced SST is not limited to surface wind speed but also quantifiable in satellite-derived cloud fraction, cloud liquid water, water vapor, and rainfall.

However, it is well known that satellite-based measurements, particularly rainfall estimates, are subject to considerable uncertainty (e.g., Arkin and Xie 1994; Joyce et al. 2004; Ebert et al. 2007). The previously identified eddy-induced precipitation response is based on rainfall products using single-sensor algorithms. For example, Frenger et al. (2013) and Byrne et al. (2015) used the rainfall measurement from the Advanced Microwave Scanning Radiometer for Earth Observing System (AMSR-E) (microwave radiometer) to identify eddy-induced rainfall response in the Southern Ocean. J. Ma et al. (2015) applied the Tropical Rainfall Measuring Mission (TRMM) Microwave Imager (TMI) rain rate to study rainfall response to eddy-induced SST variability along the Kuroshio Extension region. To the best of our knowledge, there are no published studies that have attempted to examine and compare eddy-induced rainfall using multiple satellite-based rainfall products, although many efforts have been made to compare satellite-derived precipitation estimates and their algorithms (e.g., Adler et al. 2001; Ebert et al. 2007).

Different satellite-measured products have different measurement accuracy, sampling frequency, and associated algorithms that can lead to different biases and measurement errors as well as sampling uncertainties (e.g., Arkin and Xie 1994; Adler et al. 2001; Joyce et al. 2004). Because of the limited in situ rainfall measurements over the open ocean, validating global satellite rainfall products over the oceans remains a challenge (Adler et al. 2001). Kidd et al. (2003), however, show that precipitation estimates using a multisensor algorithm are generally more accurate than using a single-sensor technique. The newly available Integrated Multisatellite Retrievals for Global Precipitation Measurement (IMERG) is based on a multisensor algorithm. It also has much improved spatial and temporal resolution over the previous products. Therefore, it is logical to hypothesize that IMERG is more suited for quantifying rainfall response to ocean eddies, which is characterized by small spatial scales and weak amplitude. The prime objective of this study is to test this hypothesis by comparing eddy-induced rainfall responses derived from IMERG and from other previous satellite-based rainfall measurements.

Understanding the effects of ocean mesoscale eddies on precipitation is vital to the understanding of frontal-mesoscale air–sea interaction, because precipitation is an integrated measure of convective processes in the atmosphere and provides an important metric for validating global and regional climate models. In this study, following Frenger et al. (2013), we will perform a composite analysis of precipitation derived from three different rainfall datasets, including the TRMM Multisatellite Precipitation Analysis (TMPA) 3B42 dataset (Huffman et al. 2007, 2010), NOAA Climate Prediction Center (CPC) morphing technique (CMORPH) global precipitation dataset (Joyce et al. 2004), and IMERG (Hou et al. 2014; Huffman et al. 2015b,c,d). The comparative analysis will be focused on eddy-active regions over the global ocean, encompassing the Kuroshio Extension, the Gulf Stream, the Agulhas Current retroflection, and the Brazil–Malvinas Confluence (four boxes in Fig. 1). The very same regions were also chosen by O'Neill et al. (2010, 2012) to analyze mesoscale air–sea interactions. We identify these four areas as the eddy-active regions based on the standard deviation maps of sea level anomaly (SLA) (not shown). In addition to the comparison of general characteristics of eddy-induced rainfall response among these three different rainfall datasets, we will examine how the rainfall response differs between summer and winter and whether the response is symmetric between cold and warm eddies.

The paper is organized as follows. Section 2 describes the datasets and analysis methods used in the study. Section 3 presents the results and discussions. Section 4 gives a summary of the major findings and discusses their implications.

2. Data and methods

a. Satellite precipitation datasets

As introduced above, three satellite-derived precipitation datasets are used in this study: TMPA, CMORPH, and IMERG. TMPA provides a quasi-global precipitation estimate consisting of both real-time (RT) and post real-time (i.e., research) products with different temporal resolutions: 3-hourly (3B42), daily (3B42 derived), and monthly (3B43). Since ocean eddies are

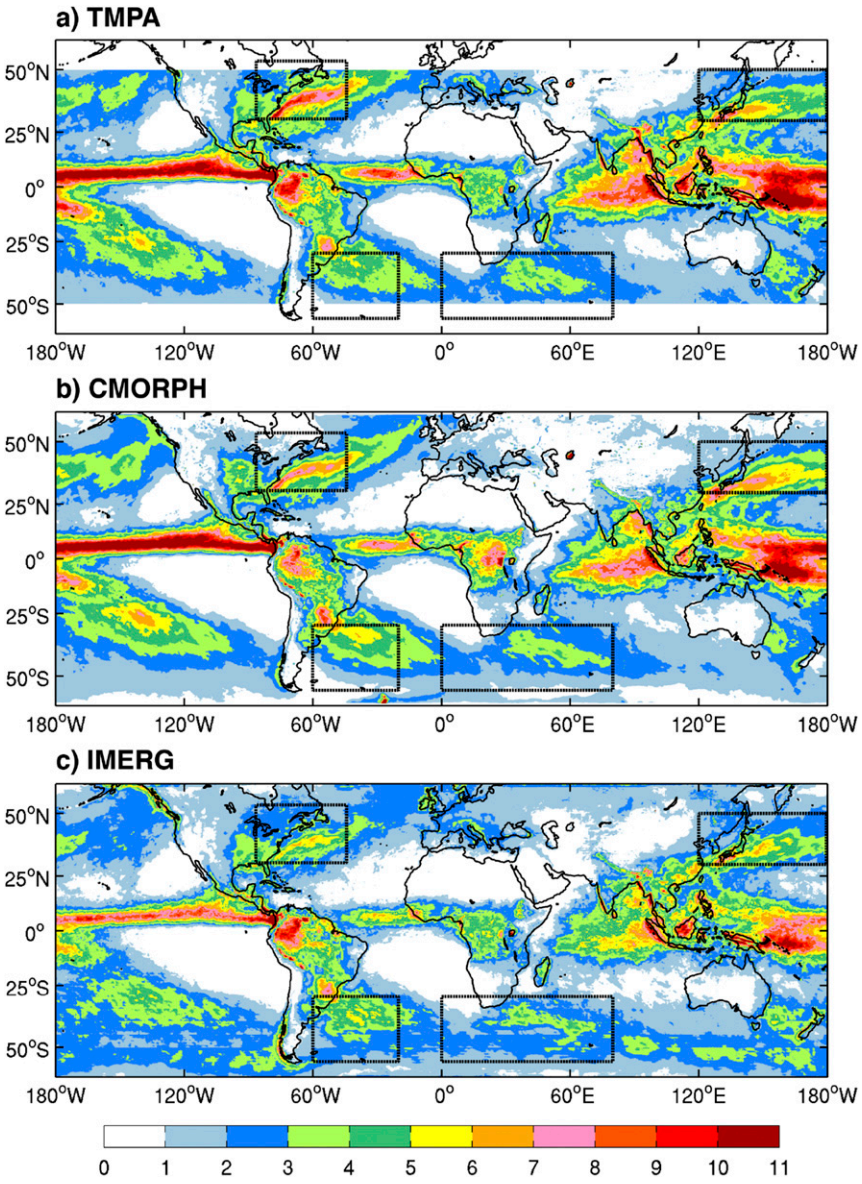

FIG. 1. April 2014–January 2016 mean rainfall derived from daily mean precipitation data (mm day^{-1}) of (a) TMPA 3B42, (b) CMORPH, and (c) IMERG. Black-dashed boxes mark the regions where eddy-induced rainfall response is analyzed.

identified using the daily merged maps of SLA, from Archiving, Validation, and Interpretation of Satellite Oceanographic Data (AVISO; Picot et al. 2003) (described later in section 2b), here the TMPA 3B42 daily product, which is a multisatellite–gauge combination, is used. It is derived based on the TRMM Combined Instrument (TCI) calibration dataset that integrates microwave measurements from TMI, AMSR-E, Special Sensor Microwave Imager (SSM/I), Special Sensor Microwave Imager/Sounder (SSMIS), Advanced Microwave Sounding Unit (AMSU), Microwave Humidity Sounder (MHS) with microwave-adjusted merged geo-infrared (IR) estimates, and monthly accumulated rain gauge analysis from Global Precipitation Climatology Centre (GPCC; Huffman et al. 2007, 2010, 2015a). The daily mean 3B42 product has a spatial resolution of 0.25° × 0.25° over 50°N–50°S from 1998 to the present.

The CMORPH dataset is derived using a morphing technique in which, instead of simply averaging microwave measurements or blending microwave and IR estimates, half-hourly low-orbiter satellite microwave–derived rainfall estimates are propagated by motion vectors estimated from IR-derived cloud properties (Joyce et al. 2004). Similar to TMPA 3B42, CMORPH is based on the

passive microwave measurements from SSM/I on board the U.S. DMSP *F13*, *F14*, and *F15* satellites, AMSU on board U.S. *NOAA-15* and *NOAA-16* satellites, and TMI aboard TRMM spacecraft. It has a temporal resolution of 3 h and spatial resolution of 0.25° × 0.25° over 60°N–60°S and is available from January 1998 to the present.

Finally, the new IMERG product unifies precipitation from a satellite constellation with the Global Precipitation Measurement (GPM) mission—a TRMM follow-on mission with significantly improved spatial resolution and coverage (Hou et al. 2014). The core observatory satellite of GPM consists of a Dual-Frequency Precipitation Radar (DPR) and GPM Microwave Imager (GMI). The dual-band precipitation radar on board the GPM satellite provides a better estimate of the sizes of precipitation particles and a wider range of precipitation rates than the single-band radar on board the TRMM satellite. The number of microwave channels is also significantly increased from 5 in the TMI to 13 in the GMI, resulting in better resolution and more reliable calibration. As a result, the GPM rainfall dataset has not only a finer spatial resolution of 0.1° × 0.1°, but also a wider range of precipitation types, including light-intensity rainfall and snowfall, than TRMM rainfall. IMERG uses more passive microwave sensors than TMPA (Huffman et al. 2015b,c,d) leading to significant changes in passive microwave rainfall estimates (Liu 2016). The IMERG algorithm (Huffman et al. 2015b,c,d) integrates multisatellite retrievals from TMPA, CMORPH, and Precipitation Estimation from Remotely Sensed Information using Artificial Neural Networks–Cloud Classification System (PERSIANN-CCS). The rain gauge analysis used is the same with TMPA from GPCC. It contains monthly and half-hourly datasets from the final run (latency ~2.5 months after the observations), the early run (5 h after observation time), and the late run (15 h after observation time). Here day 1 IMERG final run product derived from multiple satellites and gauges is used to compare with TMPA 3B42 and CMORPH. It is available from 12 March 2014 to the present with a half-hour temporal resolution.

We choose the overlapping time span of these three satellite-derived datasets from April 2014 to January 2016 to perform the comparative analysis. To test whether such a short period can provide statistically reliable results, we first analyzed and compared precipitation from TMPA 3B42 and CMORPH for the long period (in the appendix) from April 2003 to March 2014 and the short period between April 2014 and January 2016. These analyses and comparisons were also carried out separately for summer and winter. The results show that the rainfall responses derived from TMPA 3B42 and CMORPH and their differences are very similar between the long and short period. This gives us the confidence that the short overlapping period is suitable for analyzing and comparing three different rainfall datasets.

b. Eddy identification

The daily merged maps of SLA, from AVISO (Picot et al. 2003) on a uniform 0.25° × 0.25° grid from April 2003 to January 2016, were used to identify and track ocean mesoscale eddies. Following Kurian et al. (2011), we tracked eddies of effective radius, defined as the radius of a circle with the same area of the outmost closed SLA contour, between 45 and 150 km in the four eddy-active regions indicated in Fig. 1, that is, the Kuroshio Extension, the Gulf Stream, the Agulhas Current retroflection, and the Brazil–Malvinas Confluence, based on closed SLA contours from daily maps. To minimize the uncertainties in the eddy detection process, we compared the detection results against visual identification before performing a composite analysis. The identified eddies are primarily isolated ones. However, this still does not exclude the possibility that a small amount of identified eddies are bonus eddies that are filaments and transient meanders. Daily 9-km merged microwave and infrared (MW-IR) optimum interpolation (OI) of SST during the same period was used to compute SST anomalies (SSTAs) corresponding to each identified eddy. Here the eddy SSTA is defined as area-averaged SST over 1.5 eddy-radius area minus averaged SST value over an annulus between 2.5 and 1.5 eddy-radii. Using SSTA and SLA, identified eddies were grouped into warm-core anticyclonic and cold-core cyclonic rings. Since active coupling between the atmosphere and eddies occurs through SST, an SST threshold was applied to select a subset of the eddies that retain sufficiently strong SST anomalies to have an effect on the atmosphere: for each identified eddy we first computed the difference between the maximum and minimum SST within a 300 km × 300 km box aligned with the eddy center and then selected those eddies where the SST difference is larger than 2°C. A total of ~1 126 600 eddy snapshots were identified from the daily SLA and SST maps in the four eddy-active regions, and a subset of ~165 000 snapshots that coincide with the rainfall observation periods were used in the composite analysis of eddy-induced rainfall response.

c. Rainfall composite

The composite analysis follows closely that of Frenger et al. (2013). Here we highlight a few key aspects of the analysis. For each identified eddy snapshot, corresponding daily precipitation within a box of 500 km × 500 km

aligned to the eddy center was generated. Since eddies vary considerably in size, we normalized each identified eddy and its rainfall response by the eddy's radius, R. To minimize the influence from background field, we computed SST and rainfall response anomalies for each eddy by subtracting a background value surrounding the eddy from its SST and rainfall response. As noted above, the background value for SST was computed by averaging SST over an annulus of inner radius of $1.5R$ and outer radius of $2.5R$, as the SST anomaly associated with ocean eddies normally extends to $1.5R$. For rainfall, the same annulus of inner radius of $1.5R$ and outer radius of $2.5R$ was used to compute the background value, as rainfall response over each individual eddy is noisier and not always restricted within one eddy radius. We then rotated each eddy to a common westerly background wind direction, which is defined by the direction of the area-mean wind over $14R$ of the eddy, in order to distinguish the downstream and upstream responses (Frenger et al. 2013). Finally, SST and rainfall anomaly composites were made over all warm and cold eddies. Both ERA-interim daily winds at 10 m and the cross-calibrated multiplatform (CCMP), version 2, gridded daily surface winds were used to calculate the background wind direction. Because these wind products are only used to calculate the averaged wind direction over a large background area for rotating the variables, the results show little differences between them. The rainfall responses using TMPA 3B42 and CMORPH during the 11-yr period from April 2003 to March 2014 were first analyzed based on the composite of ~961 600 identified eddy daily snapshots in the four ocean frontal regions. These results were compared to the responses for the short period from April 2014 to January 2016, which contains roughly 165 000 eddy daily snapshots, to test the robustness of the finding before further comparisons were made to IMERG rainfall response.

3. Results and discussion

a. Overall rainfall characteristics

All three rainfall products exhibit an overall similar pattern of global mean precipitation (Fig. 1) characterized by the enhanced rainfall bands over the tropics and along major ocean frontal zones in the extratropics. In general, over the ocean, TMPA 3B42 and CMORPH mean rainfalls are in more agreement than that of IMERG, which is not surprising because TMPA 3B42 and CMORPH share, more or less, the same source of raw passive microwave measurements. However, there are some major discrepancies even between TMPA 3B42 and CMORPH. For example, CMORPH tends to have higher rainfall values over the Kuroshio Extension and Brazil–Malvinas Confluence than TMPA 3B42, but lower values over the Gulf Stream. These differences do not depend on the analysis period. In fact, the same differences are found between TMPA 3B42 and CMORPH in the 11-yr mean precipitation (Fig. A1 in the appendix). Among the three rainfall datasets, IMERG gives the lowest mean rainfall value (Fig. 1c) over the major oceanic precipitation regions, such as the tropics and the frontal zones. This finding is consistent with Liu (2016), who attributed the lower rainfall estimates in IMERG to changes in the passive microwave algorithms. IMERG employs more passive microwave sensors compared to TMPA, which can lead to significant changes in passive microwave rainfall estimates (Huffman et al. 2015c). Further analyses of monthly microwave and IR data indeed show that the significant differences between IMERG and TMPA are mainly caused by the different microwave products (Liu 2016). Among our four target areas, the most significant reduced rainfall estimates in IMERG occur over the Gulf Stream region, which can also be seen from Liu (2016). The lower rainfall estimate in IMERG holds for both annual mean and monthly mean patterns (not shown).

Recent studies (Tang et al. 2016; Prakash et al. 2016; He et al. 2017; Xu et al. 2017) suggest that IMERG is superior to TMPA in estimating precipitation over mainland China, India, the upper Mekong River basin, and southern Tibetan Plateau based on in situ rain gauge measurements. However, because of the lack of in situ measurements, it is difficult to validate satellite rainfall observations over the open ocean, especially in extratropical ocean frontal regions. The only one buoy we could find that was located in an extratropical ocean frontal region and also overlapped the three satellite rainfall products was the NOAA's Ocean Climate Stations Project (OCS) Kuroshio Extension Observatory (KEO) surface mooring, which is located at 32.3°N, 144.6°E. We validated the satellite rainfall products against this in situ measurement. The validation method follows Serra and McPhaden (2003). We used the averaged values of satellite-measured rainfall over a varying area ranging from a $0.1° \times 0.1°$ to $5° \times 5°$ square box centered on the KEO location to calculate rainfall statistics. Our analysis shows that the differences between KEO measurements and IMERG daily data are the smallest among the three satellite rainfall datasets (Fig. 2), which gives us the confidence that IMERG is more accurate in estimating mean precipitation over this region. The discrepancies in mean rainfall estimates raise an interesting and important question not addressed by previous studies: Do the lower mean rainfall values in IMERG translate to weaker rainfall response to ocean

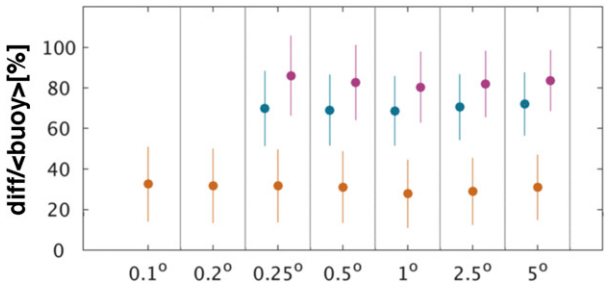

FIG. 2. Relative differences of daily mean rainfall between TMPA and the KEO buoy (cyan), between IMERG and the KEO buoy (orange), and between CMORPH and the KEO buoy (magenta) in reference to the KEO buoy mean rainfall. Satellite rainfall values are derived by averaging over various square boxes centered on the KEO buoy location whose dimension ranges from 0.1° to 5° as shown in the x axis. The dots show mean values of the relative difference and the vertical bars show 95% confidence intervals.

eddies in IMERG than in the other datasets? We address this key question of our study in section 3b.

Although lower mean values always prevail in IMERG rather than TMPA over the ocean, the systematic differences between TMPA and IMERG vary from region to region. As shown in Fig. 3, more significant differences occur over the Kuroshio Extension and Gulf Stream, and relatively small discrepancies occur over the Agulhas Current retroflection and Brazil–Malvinas Confluence. Regression analysis yields regression coefficients of 0.81 and 0.65 between CMORPH and TMPA 3B42 over the Kuroshio Extension and Gulf Stream regions, respectively, while the corresponding coefficients between IMERG and TMPA 3B42 are 0.88 and 0.61, indicating that the rainfall rate in TMPA 3B42 is systematically higher than that in CMORPH and IMERG in these two regions. Over the Agulhas Current retroflection and Brazil–Malvinas Confluence, the rainfall rate is also systematically higher in TMPA 3B42 than CMORPH and IMERG but the difference is less than 16%. These systematic differences between CMORPH and TMPA 3B42 over the four target regions remain unchanged for the 11-yr area-mean daily precipitation (Fig. A2, below), again pointing to the robustness of the results regardless of the time span considered. A comparison of rainfall probability density function (PDF) shows that TMPA tends to estimate more extreme rainfall than IMERG and CMORPH globally (not shown). Similar results hold for each individual frontal zone (not shown). At the KEO location, PDF analysis (Fig. 4) shows that TMPA and CMORPH rainfall estimates are biased low at low rain rates and high at high rain rates, while IMERG estimates always retain a better agreement with KEO measurements, indicating that the IMERG is more accurate in estimating not only the mean rainfall, but also the rainfall distribution.

b. *Response to ocean mesoscale eddies*

Because of the concern that the IMERG record is rather short and the sample size may not be sufficiently

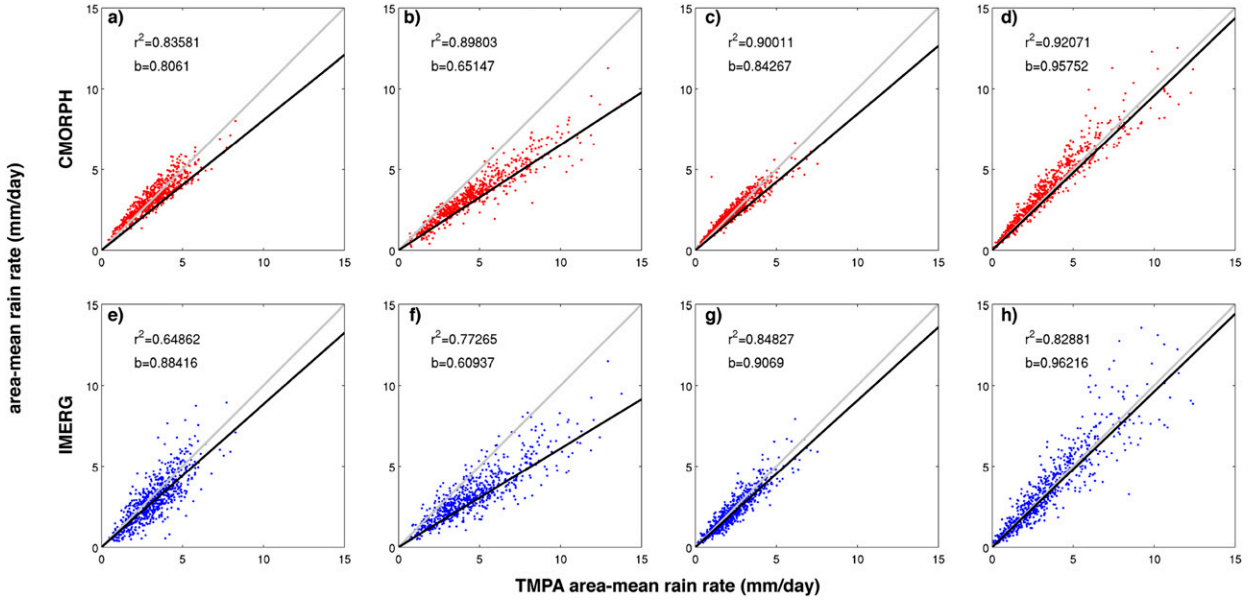

FIG. 3. Scatterplots of (top) CMORPH and (bottom) IMERG vs TMPA 3B42 area-averaged daily mean rain rates from April 2014 to January 2016 for the (a),(e) Kuroshio Extension, (b),(f) Gulf Stream, (c),(g) Agulhas Current retroflection, and (d),(h) Brazil–Malvinas confluence. The gray diagonal line in each plot indicates the one-to-one relationship and the black line is the least squares linear fit. Legends in each plot show the coefficient of determination r^2 and the slope of the linear fit b.

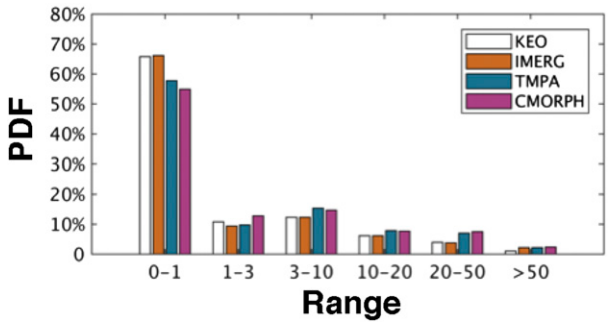

FIG. 4. PDF of daily rainfall from the KEO buoy (white), TMPA 3B42 (cyan), IMERG (orange), and CMORPH (magenta). The unit of the x axis is millimeters per day per grid.

large to distinguish the difference of rainfall responses among different rainfall datasets, we use a warm-core anticyclonic eddies minus cold-core cyclonic eddies composite to enhance the signal of rainfall response to ocean eddies by combining the sample sizes of both warm and cold eddies and to reduce background rainfall influence. However, the conclusions of the study will not change if the composite is done separately for warm and cold eddies, as will be shown below. The top panel of Fig. 5 shows composite SST and rainfall differences over all the detected anticyclonic warm-eddy snapshots (~79 700) minus the composite of all the cyclonic cold-eddy snapshots (~85 500) from April 2014 to January 2016. The composite SST is monopolar with structure similar to the composite SSH. As noted by Gaube et al. (2015), whether eddy SST has a monopolar or dipolar structure depends on eddy amplitude. For small-amplitude eddies, SST tends to have a dipolar structure because of advection of background SST by eddy currents. However, as eddy strength increases, the composite SST emerges more toward a monopole because of the increase of the rotational velocity and nonlinearity. In our target regions, large-amplitude eddies dominate mesoscale SSH variability, and therefore SST over ocean eddies tends to be monopolar rather than dipolar. Additionally, Gaube et al. (2015) show that to better illustrate the dipole SST structure, the composite needs to be calculated using a rotated coordinate that is along the orientation of the large-scale SST gradient. Otherwise, the dipole structure will be blurred because of the temporal and geographical variability in the SST gradient direction (Gaube et al. 2015). In our study, the composite is computed in a rotated coordinate determined by the large-scale winds, rather than SST gradient, to distinguish the up- and down-stream atmospheric response. All these differences can contribute to the

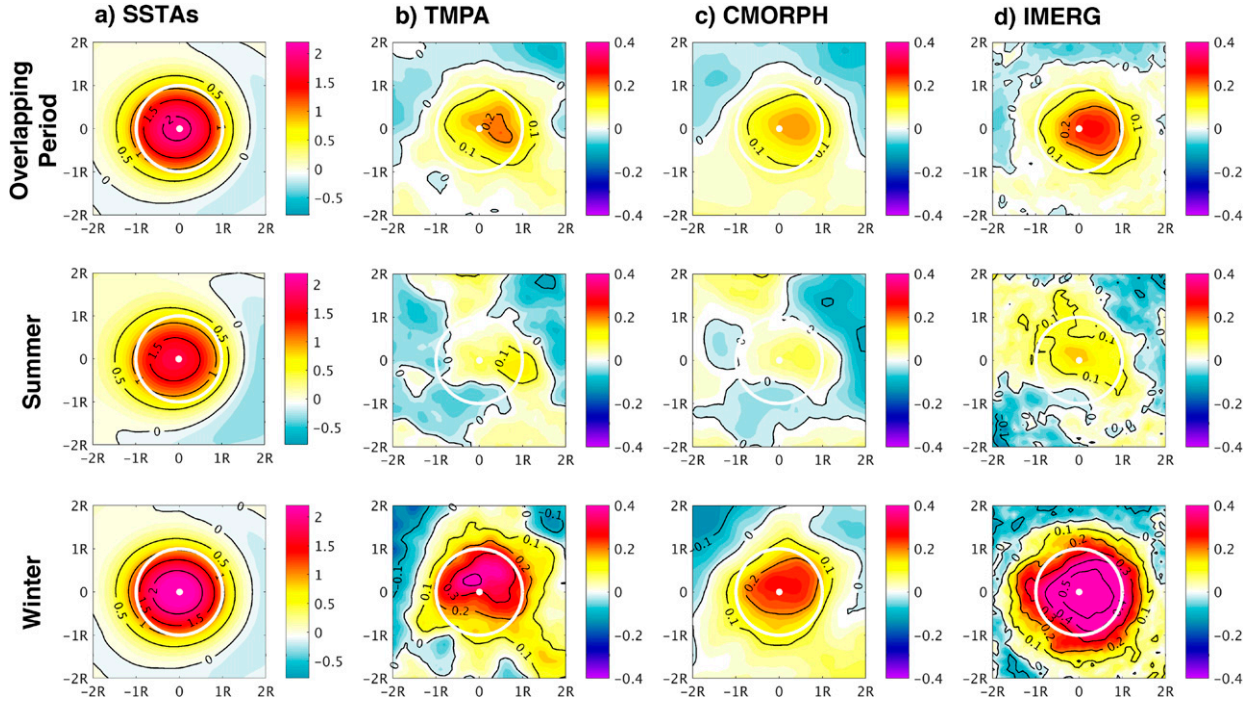

FIG. 5. Composite of normalized warm-core anticyclonic eddies minus cold-core cyclonic eddies for (a) SSTAs (contours and color; °C), (b) precipitation anomaly derived from TMPA 3B42 (contour and color; mm day^{-1}), (c) precipitation anomaly derived from CMORPH (contour and color; mm day^{-1}), and (d) precipitation anomaly derived from IMERG (contour and color; mm day^{-1}) during the (top) overlapping period, (middle) summer composites, and (bottom) winter composites. The white contour and dot in each panel mark one eddy radius and the eddy center, respectively.

monopolar structure of the composite SST in our study, which is consistent with other previous studies using similar rotated coordinates and in the same eddy active regions (Park et al. 2006; J. Ma et al. 2015; Frenger et al. 2013). The composite warm–cold-eddy SST difference shows a maximum value of about 1.8°C near the eddy center (Fig. 5a) and there is a corresponding anomalous positive rainfall composite in all three datasets. Remarkably, even though IMERG gives the weakest mean rainfall value in the regions, it reveals the strongest and most coherent rainfall response to ocean eddies (Figs. 5b–d). This result holds for each individual target region. Between the two low-resolution rainfall datasets, CMORPH gives even weaker rainfall response to eddy-induced SSTAs than TMPA—a result that again shows little dependence on the time span of the analysis (Fig. A3, below). Taken together, these findings clearly indicate that there is no relationship between mean rainfall and eddy-induced rainfall response.

The different rainfall responses to ocean eddies revealed by the three satellite-derived rainfall products can be caused by a number of factors, such as differences in sampling resolutions, sensor technologies, and retrieval algorithms, as well as analysis techniques to combine the IR data with microwave data, and so on. The weakest response in CMORPH may be caused by its morphing technique described in section 2a. As noted by Joyce et al. (2004), CMORPH can fail to detect rainfall if it forms and dissipates over areas between the paths of passive microwave instrumentations. Therefore, if eddies are located in between the overpasses of passive microwave instrumentations, it is likely that rainfall responses are underestimated by CMORPH. TMPA and IMERG, on the other hand, are based on a similar method of combining the IR data with microwave data. Some key differences between them include 1) IMERG observes a wider range of rain type from light to heavy rainfall, thanks to the DPR on board the GPM satellite, and 2) IMERG retains a much higher-resolution data than TMPA because of the larger number of microwave channels in the GMI. Either one or both of these factors can lead to the differences in the inferred rainfall response to ocean eddies.

We further analyzed and compared the rainfall response of the three satellite datasets according to different rainfall types. The definition of rain types is based on averaged rainfall values over a box of 300×300 km aligned to the eddy center. We define the value that is smaller than 3 mm day^{-1} as light rain, between 3 and 10 mm day^{-1} as moderate rain, and larger than 10 mm day^{-1} as heavy rain. The result (Fig. 6) shows that for all three datasets, the amplitude of the rainfall anomaly composite increases as rain rate increases, consistent with the notion that OME-A interactions intensify during extratropical winter storm development over active ocean-eddy regions, giving rise to stronger rainfall response to ocean eddies. Compared to TMPA and CMORPH, IMERG shows across-the-board increase in rainfall response for all rainfall types.

We computed the percentage occurrence of light, moderate, and heavy rainfall over ocean eddies, which is, respectively, ~75%, ~16%, and ~9% for IMERG, ~72%, ~16%, and ~12% for TMPA, and ~73%, ~17%, and ~10% for CMORPH. The contribution of different rain types to the rainfall responses' strength over ocean eddies, which is assessed based on the rainfall differences over warm eddies minus cold eddies, is, respectively, ~7%, ~28%, and 65% for IMERG, ~5%, ~22%, and ~73% for TMPA, and ~6%, ~26%, and ~68% for CMORPH. In all three datasets, heavy rainfall makes the most significant contribution to the rainfall responses over ocean eddies, even though its percentage occurrence is the lowest. As described above, between IMERG and other datasets, eddy-induced rainfall response strengths are discrepant. To address the question of which rainfall type contributes most significantly, we further computed the percentage contribution of each rainfall type to the corresponding total rainfall response discrepancies among these three datasets. Between IMERG and TMPA, the percentage contribution of light, moderate, and heavy rainfall difference to the total rainfall response discrepancy between them is roughly ~23%, ~26%, and ~51%, while these numbers are ~20%, ~29%, and ~52% between IMERG and CMORPH. Therefore, the largest contribution to the discrepancies in rainfall response to ocean eddies between IMERG and other two datasets appears to come from the heavy rain type.

We also conducted a sensitivity test to examine whether the rainfall response difference can be simply explained by the data resolution difference between IMERG and other datasets. To do so, we subsampled IMERG 0.1° data onto coarser grids of 0.2°, 0.3°, and 0.4°, and then repeated the rainfall response analyses. The results (Fig. 7) show that the response strength does decrease as spatial resolution decreases, but the changes are not nearly as large as those between IMERG and the other datasets. These results suggest that difference in data resolution alone cannot explain the difference in rainfall response to ocean eddies between IMERG and other datasets. It is more likely that the improvements in sensor technologies and retrieval algorithms play a key role in the stronger and more coherent rainfall response in IMERG than in other rainfall datasets. Further analysis and comparison of orbital products, which are beyond the scope of this study, can provide a better understanding of the rainfall response among different datasets.

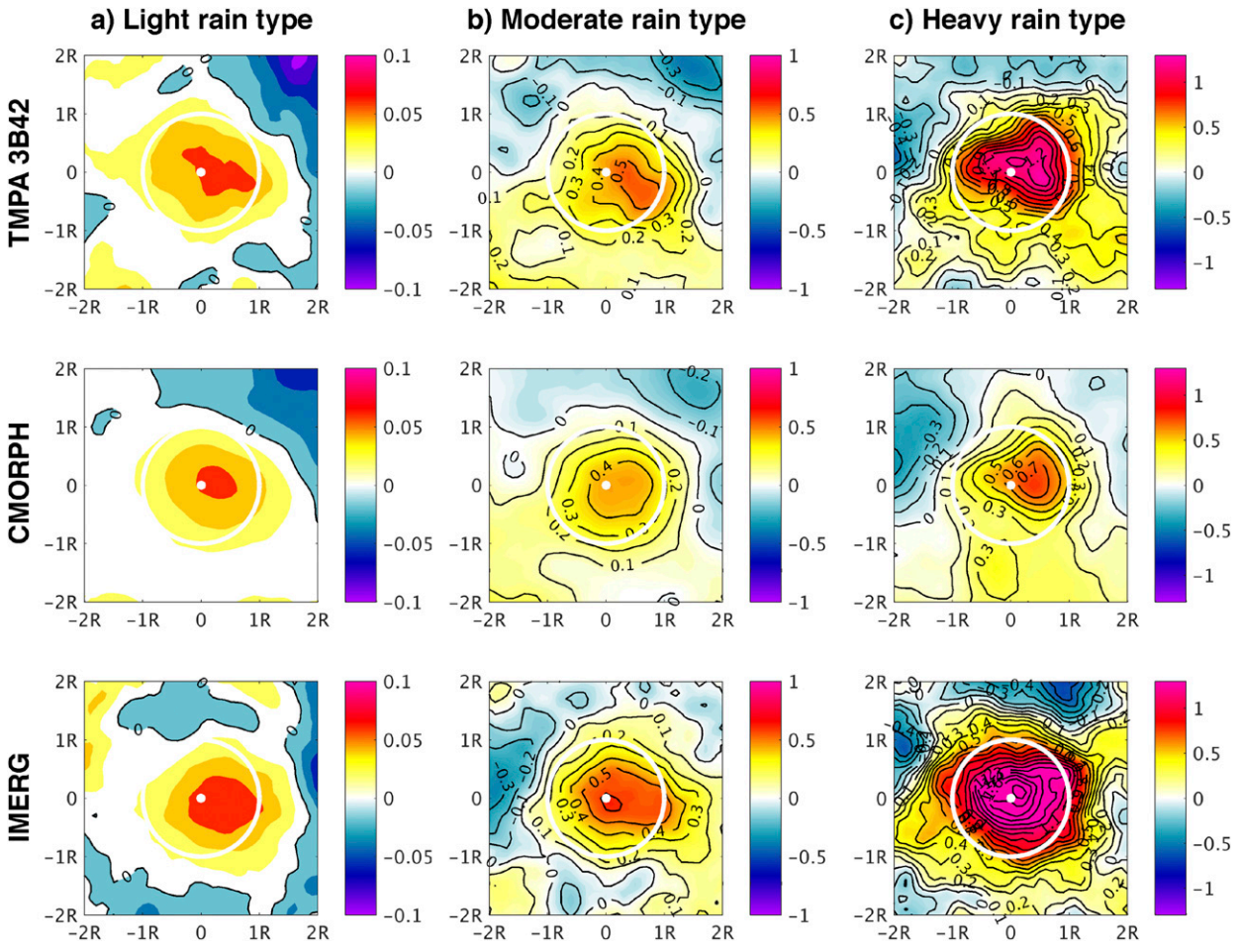

FIG. 6. Composite of normalized warm-core anticyclonic eddies minus cold-core cyclonic eddies for three rain types: (a) light, (b) moderate, and (c) heavy, from (top) TMPA 3B42, (middle) IMERG, and (bottom) CMORPH during the overlapping period. The composite method is the same as in Fig. 5. The black contour interval is 0.1 mm day^{-1}. Note that color-bar scales are different for light, moderate, and heavy rains.

c. *Response during winter and summer*

We compare summer and winter warm–cold-eddy rainfall difference composites among the three rainfall datasets during a 1-yr period from April 2014 to March 2015. Summer is defined for the months from May to September (MJJAS) for the Northern Hemisphere and from November to March (NDJFM) for the Southern Hemisphere, while winter is defined as NDJFM for the Northern Hemisphere and MJJAS for the Southern

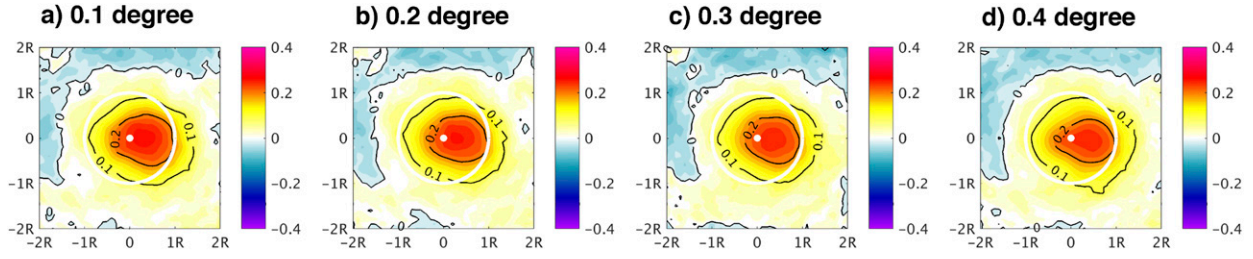

FIG. 7. Composite of normalized warm-core anticyclonic eddies minus cold-core cyclonic eddies for (a) the original 0.1° IMERG (contour and color; mm day^{-1}), (b) subsampled 0.2°, (c) 0.3°, and (d) 0.4° IMERG during the overlapping period. The composite method is the same as in Fig. 5.

Hemisphere, respectively. Consistent with the previous finding (Minobe et al. 2010), the global rainfall patterns from all datasets exhibit larger total rainfall amounts in summer than in winter. However, rainfall response PDFs show that moderate to heavy rains (>3 mm day^{-1} per grid) occur more often during winter than summer, particularly over the eddy-active frontal zones (Fig. 8). This is expected because most of the heavy rainfall is attributed to extratropical precipitating cyclones (Hawcroft et al. 2012) that are more intense and frequent during winter and interact strongly with underlying frontal and mesoscale SST over the ocean frontal zones.

We next examined and compared rainfall responses to ocean eddies between winter and summer. The SST and precipitation difference composite maps between warm and cold eddies over the four ocean frontal zones during summer and winter are shown in the middle and bottom panels of Fig. 5. Among the different rainfall products, the seasonal asymmetry in eddy-induced rainfall is most prominent in IMERG and least prominent in CMORPH. However common to all datasets, there is a well-defined asymmetry in rainfall response between winter and summer with a stronger and more coherent response in winter than in summer. This is consistent with the notion that OME-A feedback is more active in winter than in summer (e.g., Putrasahan et al. 2013).

Part of this seasonal asymmetry in rainfall response may be related to the asymmetry in ocean-eddy-induced SSTAs between summer and winter. As shown in Fig. 5, the winter SSTA composite that has maximum value of ~2.1°C and averaged value over one eddy radius of ~1.2°C is larger than the summer composite that has maximum value of ~1.5°C and averaged value over one eddy radius of ~0.9°C. However, the asymmetry in the rainfall response appears to be stronger than that in the SST. To eliminate the effect of SST difference between summer and winter, we calculated the area-averaged rainfall anomaly and SSTAs for each eddy and derived the linear regression coefficient between them. In winter, the SST–rainfall regression coefficient is ~0.51 mm day^{-1} °C^{-1} for IMERG, ~0.34 mm day^{-1} °C^{-1} for TMPA, and ~0.27 mm day^{-1} °C^{-1} for CMOPRH, while in summer, the coefficient is ~0.26, ~0.24, and ~0.22 mm day^{-1} °C^{-1}, respectively. This indicates that the rainfall response is inherently more sensitive to eddy-induced SST forcing in winter than in summer. Putrasahan et al. (2013) suggest that the seasonal sensitivity of the atmosphere to SST anomaly is associated with the vertical atmospheric stability. During winter, large averaged air–sea temperature difference contributes to a more unstable condition of the atmosphere, causing the atmosphere to be more sensitive to mesoscale SST forcing.

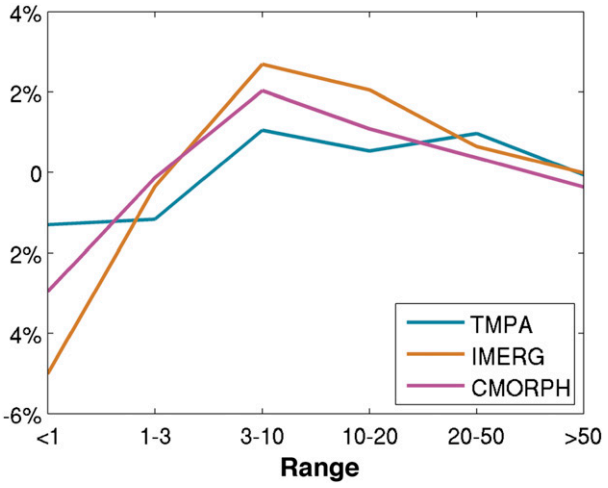

FIG. 8. Difference between winter and summer rainfall PDFs (winter minus summer) for TMPA 3B42 (cyan), IMERG (orange), and CMORPH (magenta) over extratropical eddy-active frontal zones. The unit of the *x* axis is millimeters per day per grid.

d. Response to warm-core anticyclonic and cold-core cyclonic eddies

Convective processes in the atmosphere are highly nonlinear, and thus rainfall response to warm-core anticyclonic and cold-core cyclonic eddies may exhibit different strength and sensitivity. We examine this issue by comparing rainfall responses to all warm and cold eddies in the four ocean frontal zones using three rainfall products. Figure 9 compares the warm- versus cold-eddy-induced rainfall anomaly composite during the overlapping period. IMERG shows the most pronounced asymmetry in which rainfall anomaly is considerably stronger over warm eddies than cold eddies. Less clear asymmetry is revealed by the other two rainfall datasets, although more enhanced rainfall anomaly over warm eddies than reduced rainfall anomaly over cold eddies can still be identified. This finding is further confirmed by analyzing the rainfall–SST relationship for all warm and cold eddies. Using similar regression analysis to that described in section 3c, linear regression coefficients between the area-averaged rainfall anomaly and SSTAs were calculated. The result shows that for IMERG, the SST–rainfall regression coefficient over warm eddies is nearly twice the value (~0.49 mm day^{-1} °C^{-1}) of that (~0.26 mm day^{-1} °C^{-1}) over cold eddies. For TMPA and CMORPH, the difference between the regression coefficients are smaller: the corresponding values are ~0.34 mm day^{-1} °C^{-1} (~0.23 mm day^{-1} °C^{-1}) and ~0.23 mm day^{-1} °C^{-1} (~0.20 mm day^{-1} °C^{-1}) over the warm and cold eddies from TMPA (CMORPH). Note that the regression coefficients are sensitive to the definition of the anomaly, but the relative strength of the

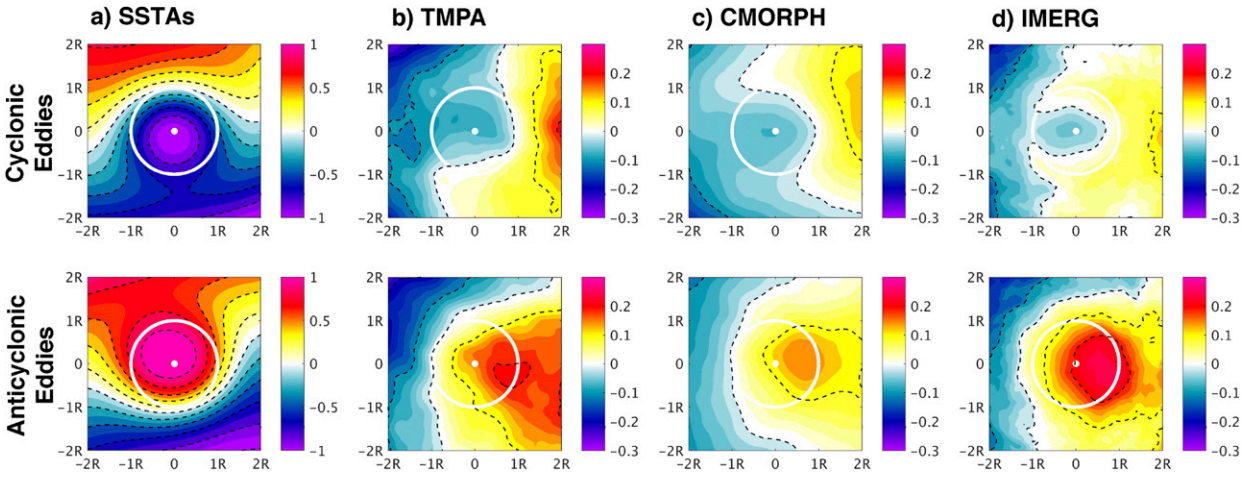

FIG. 9. Composite of (a) SSTAs (°C), (b) TMPA 3B42, (c) CMORPH, and (d) IMERG rain anomalies (mm day^{-1}) for (top) cold-core cyclonic eddies and (bottom) warm-core anticyclonic eddies during the overlapping period.

response to warm and cold eddies remains similar. These results indicate that the rainfall response is inherently more sensitive to eddy-induced warm SST anomalies.

Separate analyses for warm- versus cold-eddy-induced rainfall anomaly composite in winter (Fig. 10) and summer (Fig. 11) are also performed. A seasonal asymmetry in rainfall response with a stronger and more coherent response in winter than in summer is observed for both warm and cold eddies. However, warm eddies always tend to produce a stronger rainfall response than cold eddies. Furthermore, this asymmetry in rainfall response between warm eddies and cold eddies is most prominent in IMERG in both summer and winter compared to the other two datasets.

To further reveal the nonlinear relationship between eddy-induced SSTAs and rainfall response, a nonlinear function is fit to the scatterplot between SSTAs and rainfall anomalies across all eddies using the IMERG product (Fig. 12). An increasing slope from cold to warm eddies is clearly observed, indicating that rainfall response is stronger over warm eddies than cold eddies. This is consistent with the composite and linear regression analyses performed separately for warm and cold eddies. Similar nonlinear regression analyses are performed for summer and winter, respectively (Fig. 13). Again, in agreement with the other analyses of the study, the regression slope is larger in winter than in summer. These results reinforce the evidence that rainfall has a stronger response to eddy-induced SSTs in winter and

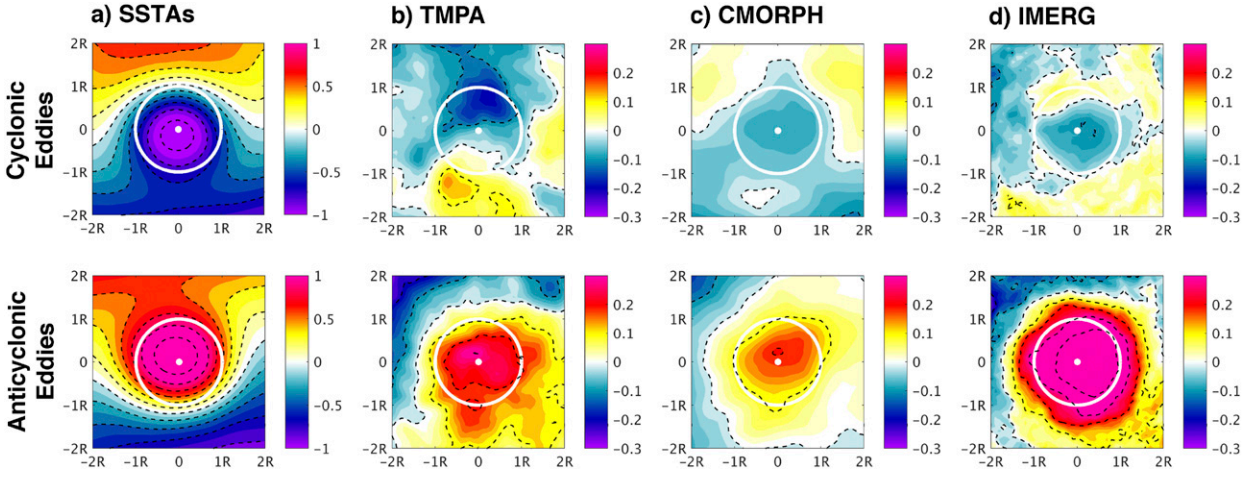

FIG. 10. As in Fig. 9, but for winter.

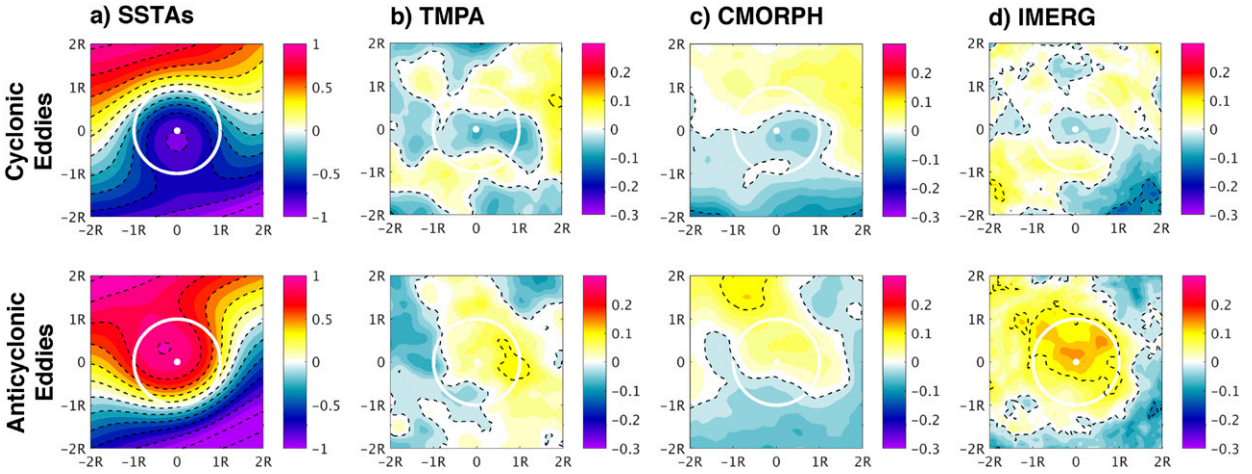

FIG. 11. As in Fig. 9, but for summer.

the nonlinearity between SSTAs and rainfall is stronger in winter than in summer.

Documenting and understanding this asymmetry in rainfall response is important, because it has a direct bearing on the question of whether ocean mesoscale eddies can have a rectified effect on the atmosphere. On average, numbers of ocean eddies are roughly evenly divided between warm anticyclones and cold cyclones. Since positive rainfall anomalies over warm eddies are generally stronger than negative rainfall anomalies over cold eddies, it suggests that eddy-induced mesoscale SST anomalies along ocean frontal zones may make a net contribution to total rainfall integrated over these regions. With the assumptions that the number of warm and cold eddies is the same and that they have about the same amplitude distributions of SSTA values, the net contribution of the ocean eddies to the overlying rainfall is estimated to be roughly 0.23 mm day^{-1} °C^{-1} (based on IMERG). Understanding this net effect of ocean eddies on the atmosphere may be a key to understanding the role of mesoscale SST in forcing large-scale atmospheric circulation, as demonstrated by some recent modeling studies (e.g., X. Ma et al. 2015).

4. Discussion and conclusions

We analyze and compare observed oceanic precipitation and its response to ocean-eddy-induced mesoscale SST using three different satellite-based rainfall datasets, TMPA, IMERG, and CMORPH, over the common period from April 2014 to January 2016. In spite of the short record length, we are able to obtain statistically robust

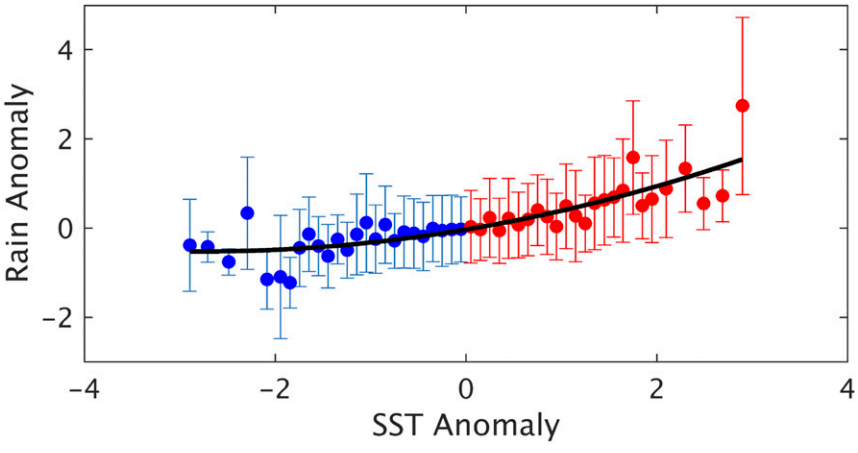

FIG. 12. Binned averages of IMERG rainfall anomaly over warm eddies (red) and cold eddies (blue). Error bar refers to standard deviation. A nonlinear fitted black line shows the response strength of rainfall anomalies to SST anomalies.

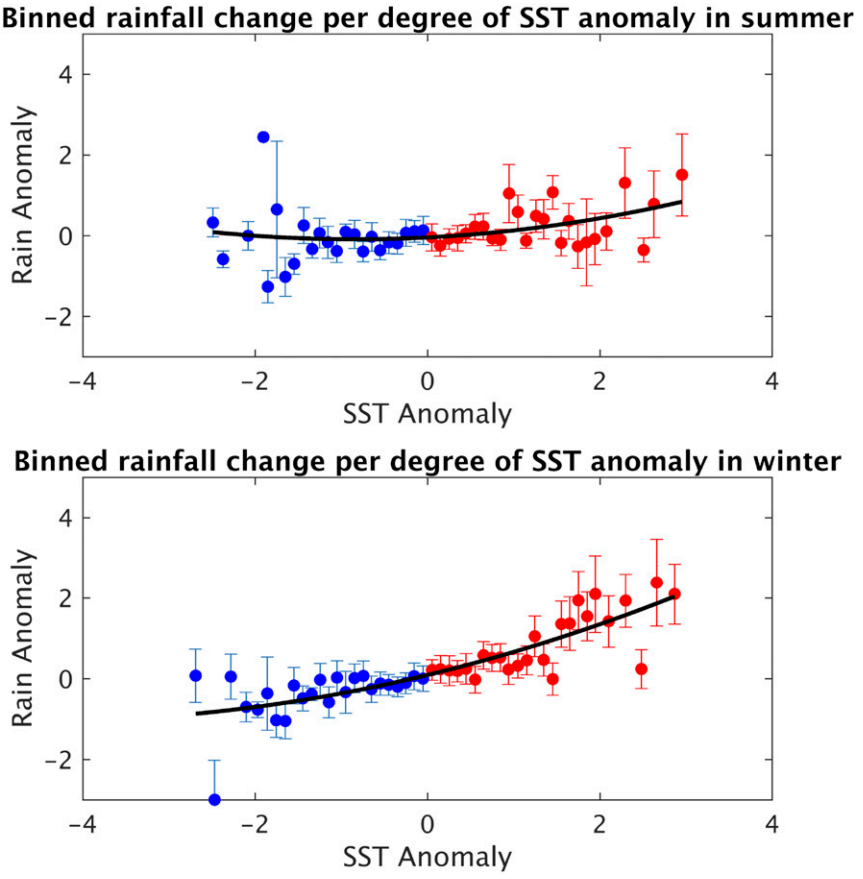

FIG. 13. Binned averages of IMERG rainfall anomaly over warm eddies (red) and cold eddies (blue) in (top) summer and (bottom) winter. Error bar refers to standard deviation. A nonlinear fitted black line shows the relationship between rainfall and SST anomalies across all eddies.

findings using composite analyses over 165 000 ocean mesoscale eddy snapshots that are identified and traced using satellite altimetry in four of the most eddy-energetic regions of the ocean. The finding shows agreement among the datasets that the atmosphere does respond to mesoscale SST forcing, producing more (less) rainfall over warm (cold) eddies. However, the response strength varies considerably from dataset to dataset, with the newly available high-resolution IMERG rainfall dataset revealing the strongest and most coherent response, despite the fact that the mean rainfall is the weakest in IMERG. It suggests that mean rainfall strength has little direct bearing on rainfall response to ocean eddies. Further analyses suggest that improvements in passive microwave sensors and algorithms together with the significantly enhanced resolution in IMERG collectively contribute to the more robust rainfall response in IMERG than the other two datasets. However, a detailed analysis and comparison of orbital products is required to understand the causes of these differences.

With the more robust rainfall response in IMERG, we are able to detect a distinct seasonal asymmetry in rainfall response to mesoscale SST forcing with a stronger response during winter than summer. This asymmetry can only be partly explained by the larger SSTAs in winter. The atmosphere is more sensitive to SST forcing during winter because the frequent passage of winter storms over the warmer ocean along the fronts reduces vertical stability of the atmosphere, enhancing OME-A feedback. This seasonal dependence underscores the importance of the interaction between atmospheric synoptic storms and ocean mesoscale eddies during winter.

Another important asymmetry that is better revealed by the higher-resolution IMERG is in the rainfall response to warm *versus* cold eddies; the former is more effective in producing positive rainfall anomalies than the latter producing negative rainfall anomalies. This is important because it suggests that atmospheric response to ocean eddies is nonlinear, which can result in a

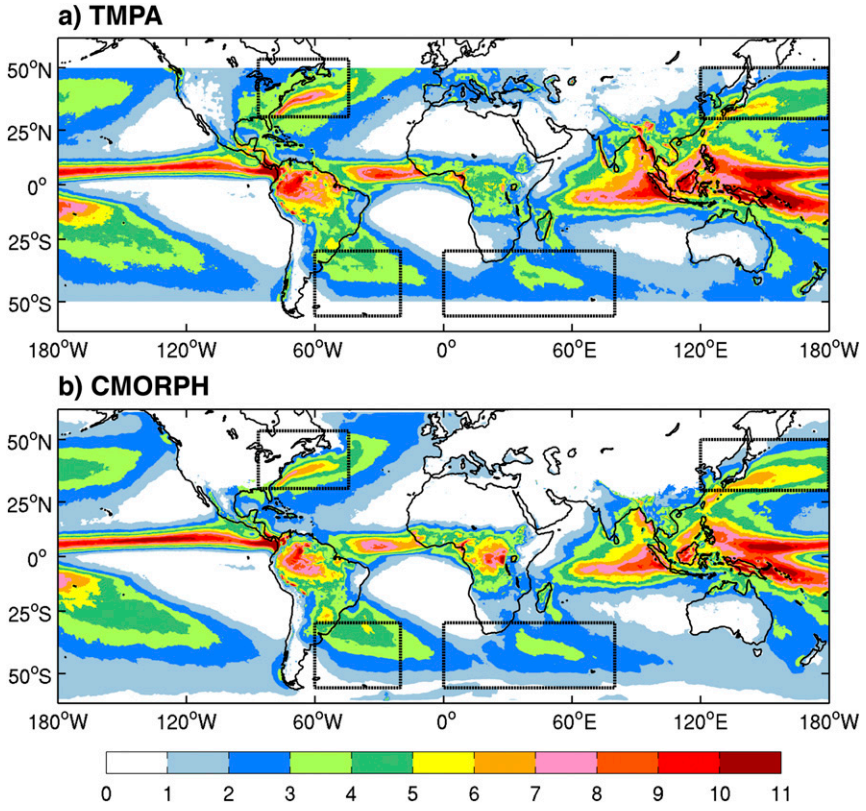

FIG. A1. The 11-yr mean rainfall (mm day^{-1}) computed from daily mean (a) TMPA 3B42 and (b) CMORPH data. Black-dashed boxes mark the regions where eddies are identified and tracked for analyzing eddy-induced rainfall response.

nonzero net effect of ocean-eddy forcing on the atmosphere at scales that are much larger than individual ocean-eddy scales. In particular, the asymmetric rainfall response suggests that ocean-eddy forcing may have a net impact on the large-scale moisture budget within the PBL and the lower atmosphere, which can potentially affect winter cyclogenesis through moist baroclinic instability or diabatic Rossby wave processes, as shown in X. Ma et al. (2015, 2017). Because satellite rainfall observations alone do not provide a way to analyze the vertical structure of atmospheric response, it is beyond the scope of this study to examine whether individual eddies can produce deep convective rainfall responses in midlatitudes. However, even if such responses are absent, we submit that eddies may still exert an influence on large-scale atmospheric circulation by affecting the lower-atmosphere and marine boundary layer moisture budget, which in turn may affect cyclogenesis and storm tracks. As such, we emphasize the importance of understanding the asymmetry of rainfall response to warm versus cold eddies and call for further investigations to understand the underlying mechanisms responsible for the asymmetric rainfall response to ocean eddies.

Finally, it is important to point out that satellite remotely sensed measurements are presently the only means of systematically observing rainfall over the extratropical oceans. However, the lack of in situ rainfall measurements over the extratropical oceans poses a great challenge for directly validating the satellite rainfall measurements, which makes it all the more important to compare different satellite rainfall products. In this study, we also validated the statistical robustness of the results by comparing the analyses between the 11-yr period that covers the entire record length of TMPA and CMORPH and the short overlapping period shared by the three datasets. The results show that the findings do not depend on the time span of the analyses. Further studies of orbital products are necessary to understand the causes of the difference among these satellite rainfall products and determine absolute errors in each of these products.

We have attempted to validate the satellite rainfall measurements against buoy rainfall measurements over the open ocean. Since our interest is in the extratropical ocean frontal region, we found only one buoy rainfall measurement located in the Kuroshio Extension region

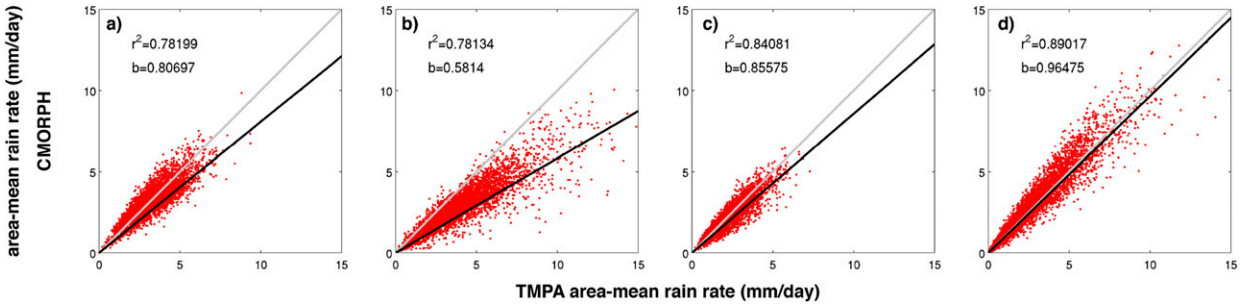

FIG. A2. Scatterplots of 11-yr CMORPH vs TMPA 3B42 area-averaged daily mean rainfall over the (a) Kuroshio Extension, (b) Gulf Stream, (c) Agulhas Current retroflection, and (d) Brazil–Malvinas Confluence. The gray diagonal line in each plot indicates the one-to-one relationship and the black line is the least squares linear fit. Legends in each plot show r^2 and the slope of the linear fit b.

that overlaps with the three satellite rainfall products. Our comparative analyses show that IMERG is superior in estimating both the mean value and the distribution of rain rate as compared to the other two satellite-derived products. Therefore, based on all the analysis results and our understanding of OME-A interaction, we conclude that IMERG gives the most reliable estimate of rainfall response to ocean eddies. We believe that this high-resolution rainfall product will be highly valuable for validating high-resolution climate model simulations and advancing our understanding of OME-A interaction.

Acknowledgments. This research is supported by U.S. National Science Foundation Grants AGS-1067937 and AGS-1347808, and National Oceanic and Atmospheric Administration Grant NA11OAR4310154. We also acknowledge the support from China's National Basic Research Priorities Programmer (2013CB956204) and the Natural Science Foundation of China (41222037 and 41221063). X. L. acknowledges the support from the China Scholarship Council. We acknowledge NASA, the NOAA, the AVISO+, the ECMWF, and the Remote Sensing Systems (RSS) for their roles in making the research data publicly available.

APPENDIX

Analysis Verification

The overlapping time span of TMPA, CMORPH, and IMERG is from April 2014 to January 2016. To verify whether this short overlapping period is suitable to perform the comparative analysis and provides statistically reliable results, we first analyzed and compared precipitation from TMPA 3B42 and CMORPH for the 11-yr-long period from April 2003 to March 2014 and the short period between April 2014 and January 2016.

Similar to Fig. 1, global mean precipitation during the long period (Fig. A1) shows enhanced rainfall over the tropics and along major ocean frontal zones in the extratropics. And the same major discrepancies between TMPA 3B42 and CMORPH are found in this long-period precipitation as in the short period: CMORPH tends to have higher rainfall values over the Kuroshio Extension

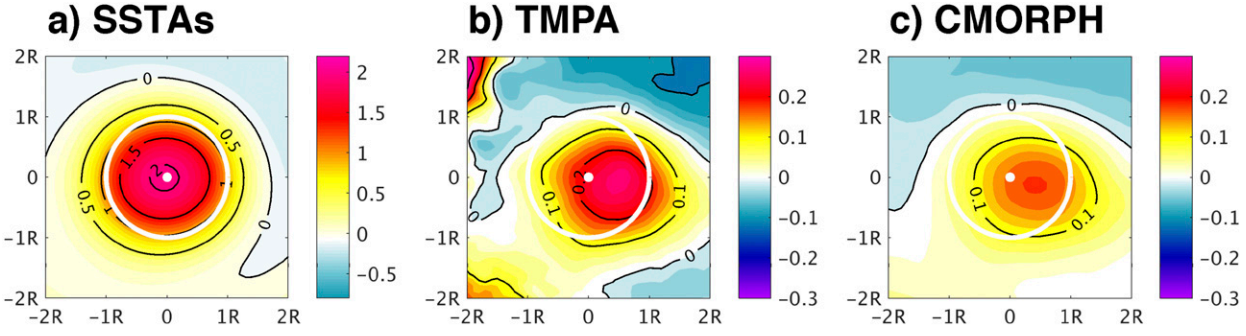

FIG. A3. Composite of 11-yr normalized warm-core anticyclonic eddies minus cold-core cyclonic eddies for (a) SSTAs (contours and color; °C), (b) precipitation anomaly derived from TMPA 3B42 (contour and color; mm day^{-1}), and (c) precipitation anomaly derived from CMORPH (contour and color; mm day^{-1}). The white contour and dot mark one eddy radius and the eddy center, respectively. The composite method is the same as in Fig. 5.

and Brazil–Malvinas Confluence but lower values over the Gulf Stream. Even the systematic differences between CMORPH and TMPA 3B42 over the four target regions remain unchanged (Fig. A2). Regression analysis yields regression coefficients of 0.81 and 0.58 between CMORPH and TMPA 3B42 over the Kuroshio Extension and Gulf Stream regions, respectively, while over the Agulhas Current retroflection and Brazil–Malvinas Confluence, the rainfall rate is only slightly systematically higher in TMPA 3B42 than CMORPH. Over this 11-yr period, ~961 600 eddy daily snapshots are identified in the four ocean frontal regions, and the composite maps (Fig. A3) of SST and rainfall shows coherent responses that rainfall is enhanced over the warm eddies. From Fig. A3, CMORPH gives weaker rainfall response than TMPA, which is consistent with the short-period results. All these analysis points to the robustness of the results regardless of the time span considered, and gives us the confidence that the short overlapping period is suitable for analyzing and comparing three different rainfall datasets.

REFERENCES

Adler, R. F., C. Kidd, G. Petty, M. Morissey, and H. M. Goodman, 2001: Intercomparison of global precipitation products: The Third Precipitation Intercomparison Project (PIP-3). *Bull. Amer. Meteor. Soc.*, **82**, 1377–1396, https://doi.org/10.1175/1520-0477(2001)082<1377:IOGPPT>2.3.CO;2.

Arkin, P. A., and P. Xie, 1994: The Global Precipitation Climatology Project: First algorithm intercomparison project. *Bull. Amer. Meteor. Soc.*, **75**, 401–419, https://doi.org/10.1175/1520-0477(1994)075<0401:TGPCPF>2.0.CO;2.

Bryan, F. O., R. Tomas, J. M. Dennis, D. B. Chelton, N. G. Loeb, and J. L. McClean, 2010: Frontal scale air-sea interaction in high-resolution coupled climate models. *J. Climate*, **23**, 6277–6291, https://doi.org/10.1175/2010JCLI3665.1.

Byrne, D., L. Papritz, I. Frenger, M. Münnich, and N. Gruber, 2015: Atmospheric response to mesoscale sea surface temperature anomalies: Assessment of mechanisms and coupling strength in a high-resolution coupled model over the South Atlantic. *J. Atmos. Sci.*, **72**, 1872–1890, https://doi.org/10.1175/JAS-D-14-0195.1.

Chelton, D. B., and S.-P. Xie, 2010: Coupled ocean-atmosphere interaction at oceanic mesoscales. *Oceanography*, **23** (4), 52–69, https://doi.org/10.5670/oceanog.2010.05.

——, M. G. Schlax, M. H. Freilich, and R. F. Milliff, 2004: Satellite measurements reveal persistent small-scale features in ocean winds. *Science*, **303**, 978–983, https://doi.org/10.1126/science.1091901.

Ebert, E. E., J. E. Janowiak, and C. Kidd, 2007: Comparison of near-real-time precipitation estimates from satellite observations and numerical models. *Bull. Amer. Meteor. Soc.*, **88**, 47–64, https://doi.org/10.1175/BAMS-88-1-47.

Frenger, I., N. Gruber, R. Knutti, and M. Münnich, 2013: Imprint of Southern Ocean eddies on winds, clouds and rainfall. *Nat. Geosci.*, **6**, 608–612, https://doi.org/10.1038/ngeo1863.

Gaube, P., D. B. Chelton, R. M. Samelson, M. G. Schlax, and L. W. O'Neill, 2015: Satellite observations of mesoscale eddy-induced Ekman pumping. *J. Phys. Oceanogr.*, **45**, 104–132, https://doi.org/10.1175/JPO-D-14-0032.1.

Hawcroft, M. K., L. C. Shaffrey, K. I. Hodges, and H. F. Dacre, 2012: How much Northern Hemisphere precipitation is associated with extratropical cyclones? *Geophys. Res. Lett.*, **39**, L24809, https://doi.org/10.1029/2012GL053866.

He, Z., L. Yang, F. Tian, G. Ni, A. Hou, and H. Liu, 2017: Intercomparisons of rainfall estimates from the TRMM and GPM multisatellite products over the upper Mekong River basin. *J. Hydrometeor.*, **18**, 413–430, https://doi.org/10.1175/JHM-D-16-0198.1.

Hou, A. Y., and Coauthors, 2014: The Global Precipitation Measurement mission. *Bull. Amer. Meteor. Soc.*, **95**, 701–722, https://doi.org/10.1175/BAMS-D-13-00164.1.

Huffman, G. J., and Coauthors, 2007: The TRMM Multisatellite Precipitation Analysis (TMPA): Quasi-global, multiyear, combined-sensor precipitation estimates at fine scales. *J. Hydrometeor.*, **8**, 38–55, https://doi.org/10.1175/JHM560.1.

——, R. F. Adler, D. T. Bolvin, and E. J. Nelkin, 2010: The TRMM Multi-Satellite Precipitation Analysis (TMPA). *Satellite Rainfall Applications for Surface Hydrology*, M. Gebremichael and F. Hossain, Eds., Springer, 3–22, https://doi.org/10.1007/978-90-481-2915-7_1.

——, and Coauthors, Eds., 2015a: The climate data guide: TRMM: Tropical Rainfall Measuring Mission. NCAR–UCAR, accessed 18 June 2015, https://climatedataguide.ucar.edu/climate-data/trmm-tropical-rainfall-measuring-mission.

——, D. T. Bolvin, D. Braithwaite, K. Hsu, R. Joyce, C. Kidd, E. J. Nelkin, and P. Xie, 2015b: NASA Global Precipitation Measurement (GPM) Integrated Multi-satellite Retrievals for GPM (IMERG). NASA Algorithm Theoretical Basis Doc., version 4.5, 26 pp., https://pmm.nasa.gov/sites/default/files/document_files/IMERG_ATBD_V4.5.pdf.

——, ——, and E. J. Nelkin, 2015c: Integrated Multi-satellite Retrievals for GPM (IMERG) technical documentation. NASA/GSFC Code 612 Tech. Doc., 48 pp., https://pmm.nasa.gov/sites/default/files/document_files/IMERG_doc.pdf.

——, ——, and ——, 2015d: Day 1 IMERG final run release notes. NASA Tech. Note., 9 pp., https://pmm.nasa.gov/sites/default/files/document_files/IMERG_FinalRun_Day1_release_notes.pdf.

Joyce, R. J., J. E. Janowiak, P. A. Arkin, and P. Xie, 2004: CMORPH: A method that produces global precipitation estimates from passive microwave and infrared data at high spatial and temporal resolution. *J. Hydrometeor.*, **5**, 487–503, https://doi.org/10.1175/1525-7541(2004)005<0487:CAMTPG>2.0.CO;2.

Kidd, C., D. R. Kniveton, M. C. Todd, and T. J. Bellerby, 2003: Satellite rainfall estimation using combined passive microwave and infrared algorithms. *J. Hydrometeor.*, **4**, 1088–1104, https://doi.org/10.1175/1525-7541(2003)004<1088:SREUCP>2.0.CO;2.

Kurian, J., F. Colas, X. Capet, J. C. McWilliams, and D. B. Chelton, 2011: Eddy properties in the California Current System. *J. Geophys. Res.*, **116**, C08027, https://doi.org/10.1029/2010JC006895.

Liu, Z., 2016: Comparison of Integrated Multisatellite Retrievals for GPM (IMERG) and TRMM Multisatellite Precipitation Analysis (TMPA) monthly precipitation products: Initial results. *J. Hydrometeor.*, **17**, 777–790, https://doi.org/10.1175/JHM-D-15-0068.1.

Ma, J., H. Xu, C. Dong, P. Lin, and Y. Liu, 2015: Atmospheric responses to oceanic eddies in the Kuroshio Extension region. *J. Geophys. Res. Atmos.*, **120**, 6313–6330, https://doi.org/10.1002/2014JD022930.

Ma, X., and Coauthors, 2015: Distant influence of Kuroshio eddies on North Pacific weather patterns? *Sci. Rep.*, **5**, 17785, https://doi.org/10.1038/srep17785.

——, and Coauthors, 2016: Western boundary currents regulated by interaction between ocean eddies and the atmosphere. *Nature*, **535**, 533–537, https://doi.org/10.1038/nature18640.

——, P. Chang, R. Saravanan, R. Montuoro, H. Nakamura, D. Wu, X. Lin, and L. Wu, 2017: Importance of resolving Kuroshio front and eddy influence in simulating the North Pacific storm track. *J. Climate*, **30**, 1861–1880, https://doi.org/10.1175/JCLI-D-16-0154.1.

Minobe, S., M. Miyashita, A. Kuwano-Yoshida, H. Tokinaga, and S.-P. Xie, 2010: Atmospheric response to the Gulf Stream: Seasonal variations. *J. Climate*, **23**, 3699–3719, https://doi.org/10.1175/2010JCLI3359.1.

O'Neill, L. W., D. B. Chelton, S. K. Esbensen, and F. J. Wentz, 2005: High-resolution satellite measurements of the atmospheric boundary layer response to SST variations along the Agulhas Return Current. *J. Climate*, **18**, 2706–2723, https://doi.org/10.1175/JCLI3415.1.

——, ——, and ——, 2010: The effects of SST-induced surface wind speed and direction gradients on midlatitude surface vorticity and divergence. *J. Climate*, **23**, 255–281, https://doi.org/10.1175/2009JCLI2613.1.

——, ——, and ——, 2012: Covariability of surface wind and stress responses to sea surface temperature fronts. *J. Climate*, **25**, 5916–5942, https://doi.org/10.1175/JCLI-D-11-00230.1.

Park, K.-A., P. Cornillon, and D. L. Codiga, 2006: Modification of surface winds near ocean fronts: Effects of Gulf Stream rings on scatterometer (QuikSCAT, NSCAT) wind observations. *J. Geophys. Res.*, **111**, C03021, https://doi.org/10.1029/2005JC003016.

Picot, N., K. Case, S. Desai, and P. Vincent, 2003: AVISO and PODAAC user handbook: IGDR and GDR Jason products. NASA JPL Tech. Doc. D-21352, 124 pp.

Prakash, S., A. K. Mitra, D. S. Pai, and A. AghaKouchak, 2016: From TRMM to GPM: How well can heavy rainfall be detected from space? *Adv. Water Resour.*, **88**, 1–7, https://doi.org/10.1016/j.advwatres.2015.11.008.

Putrasahan, D. A., A. J. Miller, and H. Seo, 2013: Isolating mesoscale coupled ocean–atmosphere interactions in the Kuroshio Extension region. *Dyn. Atmos. Oceans*, **63**, 60–78, https://doi.org/10.1016/j.dynatmoce.2013.04.001.

Serra, Y. L., and M. J. McPhaden, 2003: Multiple time- and space-scale comparisons of ATLAS buoy rain gauge measurements with TRMM satellite precipitation measurements. *J. Appl. Meteor.*, **42**, 1045–1059, https://doi.org/10.1175/1520-0450(2003)042<1045:MTASCO>2.0.CO;2.

Small, R. J., and Coauthors, 2008: Air–sea interaction over ocean fronts and eddies. *Dyn. Atmos. Oceans*, **45**, 274–319, https://doi.org/10.1016/j.dynatmoce.2008.01.001.

Tang, G., Y. Ma, D. Long, L. Zhong, and Y. Hong, 2016: Evaluation of GPM Day-1 IMERG and TMPA version-7 legacy products over mainland China at multiple spatiotemporal scales. *J. Hydrol.*, **533**, 152–167, https://doi.org/10.1016/j.jhydrol.2015.12.008.

Tokinaga, H., Y. Tanimoto, and S.-P. Xie, 2005: SST-induced surface wind variations over the Brazil–Malvinas confluence: Satellite and in situ observations. *J. Climate*, **18**, 3470–3482, https://doi.org/10.1175/JCLI3485.1.

Xie, S.-P., 2004: Satellite observations of cool ocean–atmosphere interaction. *Bull. Amer. Meteor. Soc.*, **85**, 195–208, https://doi.org/10.1175/BAMS-85-2-195.

Xu, R., F. Tian, L. Yang, H. Hu, H. Lu, and A. Hou, 2017: Ground validation of GPM IMERG and TRMM 3B42V7 rainfall products over southern Tibetan Plateau based on a high-density rain gauge network. *J. Geophys. Res. Atmos.*, **122**, 910–924, https://doi.org/10.1002/2016JD025418.